chemosensors

Article

The Effect of Doping rGO with Nanosized MnO_2 on Its Gas Sensing Properties

Mohamed Ayoub Alouani [1,2,3], Juan Casanova-Chafer [4], Santiago de Bernardi-Martín [5], Alejandra García-Gómez [5], Foad Salehnia [1,2,3], José Carlos Santos-Ceballos [1,2,3], Alejandro Santos-Betancourt [1,2,3], Xavier Vilanova [1,2,3,*] and Eduard Llobet [1,2,3,*]

1 Department of Electronic Engineering, School of Engineering, Universitat Rovira i Virgili, MINOS, Avda. Països Catalans 26, 43007 Tarragona, Spain; mohamedayoub.alouani@urv.cat (M.A.A.); foad.salehnia@urv.cat (F.S.); josecarlos.santos@urv.cat (J.C.S.-C.); alejandro.santos@urv.cat (A.S.-B.)
2 IU-RESCAT, Research Institute in Sustainability, Climatic Change and Energy Transition, Universitat Rovira i Virgili, Joanot Martorell 15, 43480 Vila-seca, Spain
3 TecnATox—Centre for Environmental, Food and Toxicological Technology, Universitat Rovira i Virgili, Avda. Països Catalans 26, 43007 Tarragona, Spain
4 Research Institute for Materials Science and Engineering, Université de Mons, Avenue Copernic 3, 7000 Mons, Belgium; juan.casanova@umons.ac.be
5 Gnanomat. C/Faraday 7, 28049 Madrid, Spain; santiago.bernardi@gnanomat.com (S.d.B.-M.); alejandra.garcia@gnanomat.com (A.G.-G.)
* Correspondence: xavier.vilanova@urv.cat (X.V.); eduard.llobet@urv.cat (E.L.)

Abstract: Manganese dioxide (MnO_2) has drawn attention as a sensitiser to be incorporated in graphene-based chemoresistive sensors thanks to its promising properties. In this regard, a rGO@MnO_2 sensing material was prepared and deposited on two different substrates (silicon and Kapton). The effect of the substrate nature on the morphology and sensing behaviour of the rGO@MnO_2 material was thoroughly analysed and reported. These sensors were exposed to different dilutions of NO_2 ranging from 200 ppb to 1000 ppb under dry and humid conditions (25% RH and 70% RH) at room temperature. rGO@MnO_2 deposited on Kapton showed the highest response of 6.6% towards 1 ppm of NO_2 under dry conditions at RT. Other gases or vapours such as NH_3, CO, ethanol, H_2 and benzene were also tested. FESEM, HRTEM, Raman, XRD and ATR-IR were used to characterise the prepared sensors. The experimental results showed that the incorporation of nanosized MnO_2 in the rGO material enhanced its response towards NO_2. Moreover, this material also showed very good responses toward NH_3 both under dry and humid conditions, with the rGO@MnO_2 sensor on silicon showing the highest response of 18.5% towards 50 ppm of NH_3 under 50% RH at RT. Finally, the synthetised layers showed no cross-responsiveness towards other toxic gases.

Keywords: reduced graphene oxide; manganese dioxide (MnO_2); gas sensor; NO_2 detection; NH_3 detection; Kapton; SiO_2/Si

Citation: Alouani, M.A.; Casanova-Chafer, J.; de Bernardi-Martín, S.; García-Gómez, A.; Salehnia, F.; Santos-Ceballos, J.C.; Santos-Betancourt, A.; Vilanova, X.; Llobet, E. The Effect of Doping rGO with Nanosized MnO_2 on Its Gas Sensing Properties. *Chemosensors* **2024**, *12*, 256. https://doi.org/10.3390/chemosensors12120256

Received: 18 October 2024
Revised: 2 December 2024
Accepted: 4 December 2024
Published: 6 December 2024

1. Introduction

Technological and economic advances increasingly threaten the environment and air quality, necessitating urgent solutions. The demand for low-cost and effective gas sensors, crucial for detecting toxic agents such as nitrogen dioxide NO_2 [1], ammonia NH_3 [2], and carbon monoxide CO [3] in various fields, has never been more pressing. While traditional methods like infrared spectrophotometry (IRSP) [4], non-dispersive infrared analysis (NDIR) [5], and gas chromatography-mass spectrometry (GC-MS) [6] have been widely used for detecting toxic gases, they are not without significant drawbacks. Their high cost and complexity have underscored the need for a new, more efficient approach. This realisation has led to the development of chemoresistive devices, known for their ease of operation, low production cost, fast response time, and ease of miniaturisation [7].

Since their first use in the 1960s, metal oxides (MO_X) such as ZnO [8,9], SnO_2 [10,11], WO_3 [12,13], and many more [14] have been studied as sensitive films to be used in the fabrication of chemoresistive devices for gas sensing and especially for detecting NO_2. Even though MO_X are effective and sensitive, the need for a pervasive, widespread monitoring of air pollutants has oriented research to the discovery of new, less power-hungry, gas-sensitive materials. This has, for example, led to the emergence of graphene-based chemoresistive sensors. The unique and exceptional properties of graphene that made it a solid gas sensing material candidate are thermal stability, mechanical robustness, high conductivity, high carrier mobility at low to room temperatures, a large surface area of up to 2630 m^2/g for single-layer graphene, low electrical noise [15] and, most importantly, the fact that its electronic properties are easily affected by the adsorption of gas molecules [16]. Graphene, as a chemoresistive layer, is a p-type material. The interaction between a reducing gas such as NH_3 and the already adsorbed oxygen species on the surface of the graphene layer results in a transfer of electrons back to the surface, hence the increase in the surface resistance of the graphene film [17]. Meanwhile, when in contact with an oxidising gas such as NO_2, the transfer of electrons happens from the sensitive layer to the adsorbed NO_2 molecules, leading to a decrease in the surface resistance [18]. Table 1 displays a collection of works found in the literature using graphene-based chemoresistive sensors doped with different MO_X for the gas detection of different analytes:

Table 1. Gas sensors fabricated from graphene-based materials and their response towards different toxic gases.

Material	Target Gas	Gas Concentration (ppm)	Operating Condition	Response (%)	Ref.
Graphene/MoS_2 hybrid aerogel	NO_2	0.5	200 °C	9	[19]
rGO/SnO_2 nanoparticles	NO_2	5	50 °C	3.31	[20]
ZnO nanorods/rGO) mesoporous nanocomposites	NO_2	1	RT	119	[21]
Graphene nanoplatelets/polyaniline nanocomposite	NH_3	1	RT	0.7	[22]
rGO/PtNPs nanocomposite	NH_3	1	RT	2.87	[23]
Polyaniline (PANI)/graphene oxide (GO)/ZnO hybrid LbL film	NH_3	50	65% RH	3	[24]
Graphene oxide	H_2	200	RT	10	[25]
rGO/TiO_2 decorated by Pd/Pt nanoparticles	H_2	500	180 °C	92%	[26]

One of the graphene derivatives is reduced graphene oxide (rGO). It was reported in the literature to be the best and most used graphene-based sensing material for detecting NO_2 [27,28] and NH_3 [29,30] due to its numerous defect sites and functional groups, which facilitate gas adsorption. rGO has been reported to be able to detect chemical warfare agents and explosives at trace levels (ppb) [31]. Moreover, the synthesis of rGO can be achieved via straightforward and inexpensive processes that reduce GO via chemical and thermal routes or even using UV light [32]. Studies have shown that pristine rGO gas sensors exhibit slow response and recovery dynamics. Hence, the hybridisation of rGO with MO_X has been a solution often explored to enhance its sensing properties (e.g., ameliorating response dynamics and extending the number of gases that can be detected). D. Tripathi et al. explored this process, and an enhancement of the sensitivity and selectivity of the rGO material towards ammonia by incorporating WO_3 nanomaterial in the sensing layer was achieved [33]. Another reported work by D. Milad et al. showed that the synthesis of a TiO_2/rGO composite exhibited improved gas sensing properties towards methanol and ethanol [34]. This is achieved via the MO_X nanoparticles supported on rGO behaving as catalysts or as electronic sensitisers, favouring the occurrence of heterojunctions at the MO_X/rGO interface.

Some of the reported MO_X nanoparticles used for the loading of the rGO layers for gas sensing are ZnO [35], SnO_2 [36], and WO_3 [37]. Still, in recent years, MnO_2 has gained popularity due to its low toxicity, low cost, high stability, and ease of fabrication. It was also used in a wide range of applications and fields such as energy storage [38], biomedical field [39], and in developing gas sensors [40]. However, in the gas sensing field, there is a limited amount of reported work discussing the incorporation of the MnO_2 nanomaterial into rGO to achieve a sensitive layer towards different toxic gases. One of the few works reported is of Hui Zhang et al., where they successfully synthesised an rGO-coated Ni foam-supported MnO_2 for the enhanced detection of NO_2 at a concentration of 50 ppm while the sensor was operated at room temperature [41]. Meanwhile, Alexander et al. modified rGO with doping of MnO_2 nanoparticles and tested the rGO/MnO_2 composite as a gas sensor for different gases such as 25 ppm of NO_2, 500 ppm of H_2 and 1000 ppm of CH_4 under dry conditions with heating at 85 °C [42]. Another reported work was of Ghosal et al., where they prepared different hybrids for alcohol vapour detection. One of the hybrids, the rGO/MnO_2 nanoflowers binary composite, showed good responses towards ethanol and methanol vapours in the range of 5–100 ppm while heating at 150 °C [43]. Lastly, Ahmad et al. made a ternary nanocomposite of PANI@rGO@MnO_2 using a multi-step process for NH_3 detection. The tests were made at 100 °C under dry conditions [44]. The fact that very few works have been reported on rGO@MnO_2 gas sensors so far makes exploring its gas-sensing properties interesting and worthwhile.

In this paper, rGO@MnO_2 sensitive layers were successfully synthesised and deposited on different transducing substrates (Kapton and silicon with gold electrodes). The gas sensing performance of the rGO@MnO_2 sensors was studied for different reducing and oxidising species. The effect of ambient moisture on sensor response was evaluated as well. Results are presented and thoroughly discussed. A sensing mechanism for the detection of ammonia and nitrogen dioxide is presented.

2. Materials and Methods

In this section, a detailed explanation of the preparation of the doped reduced graphene oxide with nanosized MnO_2 at 95/5 wt.%, alongside the process of depositing it on the Kapton and silicon substrates via the spray coating technique, is presented. The section also describes the techniques employed in the study of the morphology and composition of the hybrid material and in the test of its gas sensing properties.

2.1. Preparation of Reduced Graphene Oxide Doped with MnO_2

Commercial rGO obtained from LayerOne company (Norway) was doped with nanosized MnO_2 (rGO/MnO_2 95/5 wt.%) using a process based on patented procedures (Patent number ES2678419A1) by GNANOMAT company. Briefly, reduced graphene oxide was dispersed in oxalic acid, in which the starting Mn_3O_4 had been previously dissolved at 50 °C. After homogenisation, nanosized MnO_2 was slowly precipitated on reduced graphene oxide by adding a basic solution (NaOH 5 M) under vigorous agitation. The solid was filtered and dried at 90 °C overnight. Synthesis parameters, such as temperature, stirring speed, addition rate, or MnO_2/rGO proportion, were controlled to obtain the desired crystallinity that provides the material with optimal properties. The manganese oxide phase was checked via XRD; Figure S1 (in Supplementary Materials) shows the XRD diffractogram.

2.2. Substrates Choice, Preparation, and Material Deposition

The substrate material choice was based on several factors. Kapton substrate is considered important in the synthesis of new flexible and wearable sensors since it has a very high flexibility. Ilghar R. et al. used this material as a substrate to fabricate a wearable Kapton graphene biosensor for the detection of toxic gases [45]. Additionally, Kapton has very good thermal stability and is known to be a hydrophobic material. Meanwhile, SiO_2/Si substrates have different advantages to offer. Initially, the substrate starts as a

silicon wafer and an insulating layer of SiO_2 is usually obtained via a thermal oxidation process. Such substrates show very high thermal stability and standard processes from the semiconductor industry can be used to pattern interdigitated electrodes or heating resistors.

Ten milligrams of the rGO@MnO_2 was weighed and suspended in a 10 mL ethanol solution via a 30 min sonication. Subsequently, suspended material was deposited by spray coating onto two different substrates (i.e., silicon and Kapton). During the coating process, substrates were heated at 50 °C to promote the evaporation of the solvent and the formation of a homogeneous film. Both substrates were prepared differently. The SiO_2/Si substrate was prepared by thermally growing SiO_2 on top of the silicon wafer and later cut in specific dimensions, as shown in Figure 1a, with a thickness of 0.5 mm. Meanwhile, the Kapton substrate was prepared by sticking the Kapton piece to a small plastic support with dimensions same as the silicon one shown in Figure 1b with a total thickness of 0.58 mm.

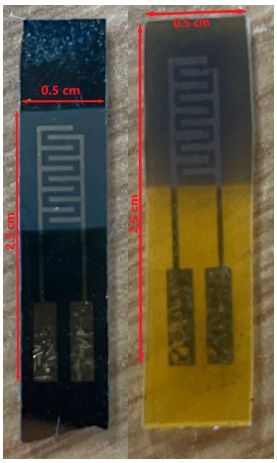

(**a**) (**b**)

Figure 1. Pictures of the prepared sensors on the (**a**) silicon substrate and (**b**) Kapton substrate.

The interdigitated gold electrodes were deposited on the substrates using different processes. For Kapton substrates, 9 nm of gold was sputtered using a shadow mask to form the electrodes. In contrast, a two-step approach was used for the silicon substrates. At first, a laser lithography technique (DWL 66fs, Heidelberg Instruments, Heidelberg, Germany) was used to pattern a photoresist that coated an oxidised silicon wafer in the shape of the electrodes. In the second step, a titanium adhesion layer was sputtered with a thickness of 10 nm, and then a gold layer was sputtered on top with a thickness of 100 nm. A final lift-off process was conducted to obtain the electrodes. The silicon wafer was then diced. Both fabricated substrates have the same configurations regarding the electrodes, which are listed below in Table 2.

Table 2. Configurations of the electrodes of the fabricated sensors.

Parameter	Dimension
Electrodes dimension	15.00 × 2.87 nm
Active area dimension	2.78 × 6.00 mm
Size of fingers	0.216 mm
Number of fingers	5
Gap between fingers	0.3 mm

2.3. Material Characterisation and Gas Sensing Measurements

A set of numerous characterisation techniques was used to study the different morphological and sensing aspects of the synthesised materials. To assess their crystallinity, a Raman spectrometer (Renishaw, plc., Wotton-under-Edge, UK) via a green laser with a wavelength of 514 nm was used. The morphology of the surface and the nanosized

material's distribution were studied using a Field Emission Scanning Electron Microscope (FESEM) employing a Carl Zeiss AG-Ultra 55 (ZEISS, Jena, Germany). A JEOL F200 TEM ColdFEG (Tokio, Japan) operated at 200 kV was used for the high-resolution transmission electron microscopy (HRTEM) characterisation. TEM images and electron diffraction patterns were acquired with a Gatan OneView camera, a CMOS-based and optical fibre-coupled detector of 4096 by 4096 pixels. Gatan Digital Micrograph program was used to process the (S)TEM images. STEM images (1024 × 1024 pixels) were recorded from the JEOL bright-field (BF) and high-angle annular dark-field (HAADF) detectors with a camera length of 200 mm. Samples were inserted in a JEOL beryllium double-tilt holder for energy-dispersive X-ray spectroscopy (EDS). STEM-EDS mapping was recorded from an EDS Centurio detector (silicon drift) with an effective area of 100 mm^2 and 133 eV of energy resolution. STEM-EDS maps (512 × 512 pixels) were processed with the JEOL Analysis software to check the shape of the nanosized MnO_2 and its incorporation in the graphene layers. Finally, a Jasco FTIR/IR-6700 infrared spectrometer (Oklahoma City, OK, USA) with a diamond crystal kit was used to conduct the ATR-IR analysis of the interaction between the molecules of the rGO@MnO_2 material. The obtained sensors were placed in a 35 cm^3 volume Teflon chamber. Later, a set of Bronkhorst mass-flow controllers (Ruurlo, The Netherlands) with a 100 mL/min flow were used to pass a continuous stream of dry air (Air Premier, 99.995% purity) and other target analytes with different concentrations through the Teflon chamber. The same set of mass flow controllers was utilised to dilute the target gases from calibrated bottles (NO_2-1 ppm, CO-100 ppm, NH_3-100 ppm, ethanol-20 ppm, and Benzene-10 ppm balanced in dry air). The resistance changes were obtained in real-time via an Agilent HP 34972A multimeter (Santa Clara, CA, USA). The ambient moisture effect on the responses of the sensors was evaluated by using a controller evaporator mixer (CEM) to obtain low humidity levels with a minimum of 25% RH and a maximum of 50% RH at room temperature. For higher values of relative humidity, the flow of the dry air with the corresponding concentration of gas was humidified, passing through a bubbling water system at room temperature. The sensing response is defined as the relative change in resistance and was calculated using the following formula:

$$R\ (\%) = ((|R_g - R_a|)/R_a) \times 100$$

R_g and R_a correspond respectively to the resistance values prior to and following gas exposure. Figure 2 shows the schematic representation of the gas detection process and equipment used.

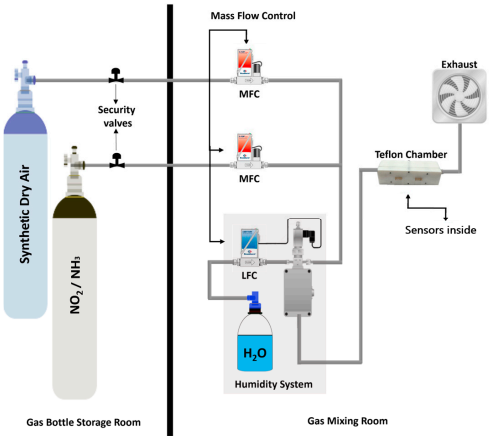

Figure 2. Schematic representation of the gas detection process and used equipment.

3. Results

This section first presents and discusses the results of the characterisation tests made for the prepared sensitive layers (rGO and rGO@MnO_2), which are based on the Raman, FESEM and HRTEM techniques. Secondly, the gas testing results for these sensors towards

NO_2 and NH_3 at room temperature under dry conditions are presented, followed by the results gathered at different humidity levels. Additionally, selectivity tests are reported. The results of the gas sensing tests are compared to those found in the literature. Finally, a sensing mechanism for the detection of NO_2 and NH_3 is introduced.

3.1. Sensitive Layer Characterisation

3.1.1. Raman

The study of the molecular structure of carbon products and the assessment of disorders and defects in the material can be performed using Raman spectroscopy analysis. Two specific peaks always appear when analysing graphene: the G-band and the D-band. The first one, placed at around 1500 cm^{-1}, corresponds to the first order scattering of the E_2g phonons at the Brillouin zone centre and originates from the in-plane vibrations of the sp^2 carbon atoms [46]. Meanwhile, the D-band is observed around 1300 cm^{-1} and represents the formation of j-point photons of A_1g symmetry; it is also associated with double bonds C=C, meaning the more intense the band is, the higher the presence of sp^2 domains is. Furthermore, D-band peak intensity depends highly on the presence of disorders and defects like vacancies and edges in the carbon lattice and grain boundaries [47]. To determine the degree of oxidation of the graphene, a simple calculation of the intensity ratio of both the D and G band peaks is enough, i.e., ID/IG; the higher this ratio is, the lower the oxidation level is [48].

Finally, the second-order bands are observed from 2500 cm^{-1} to 3200 cm^{-1}, containing one always visible peak at around 2700 cm^{-1}, known as the 2D band. They are used generally to determine the layers of the graphene since graphene is susceptible to stacking [49]. The chosen name of this band comes from the fact that it is the overtone of the D band, and two of the same phonons responsible for the D band are involved in the 2D band. Two other bands are sometimes reported when studying graphene Raman spectra, which are the D+G band, which can be seen around 2900 cm^{-1}, and the combined overtone of the D and G bands, the 2G band around 3200 cm^{-1}, which is attributed to the overtone of the G band [50]. In our case, we are working with rGO, which means that the stacking of the layers is random, and since the width of the peaks is relative to the disorder, that can lead to an overlapping of the 2D band peak with the D+G and 2G, resulting in a bump like peak observed in the range of 2600 cm^{-1} to 3100 cm^{-1} [51].

Figure 3a,b shows the Raman spectra of bare rGO and rGO doped with nanosized MnO_2, respectively. For both cases, D bands are located at 1355 cm^{-1} and G bands around 1590 cm^{-1}. For the second-order bands, three visible peaks corresponding to the 2D, D+G, and 2G bands at respectively 2697 cm^{-1}, 2940 cm^{-1}, and 3188 cm^{-1} are present in the Raman spectra of the reduced graphene oxide; meanwhile, in the Raman spectra of the MnO_2 doped reduced graphene oxide we observe a bump-like peak around 2926 cm^{-1}, which is in agreement with the explanation made previously. Moreover, the ID/IG intensity ratio is 0.89 for rGO@MnO_2 and 0.85 for rGO, showing a slightly lower oxidation level in the doped rGO and the presence of a higher number of defects, which can be caused by the doping process. Finally, it was noticed that the Raman signal in the rGO@MnO_2 sample shows a higher intensity than the pristine rGO sample, which can be correlated to the presence of the nanosized MnO_2 since the presence of MO_X usually leads to this increase in the intensity [52].

3.1.2. FESEM

Figure 4a shows the obtained FESEM images of the layers present on the surface of the graphene loaded with MnO_2 on the silicon substrate using a back-scattered electron detector (BSE). A very homogenous layer is observed covering the totality of the surface inspected. MnO_2 cannot be clearly seen, even when using a BSE detector, because of the low concentration of the nanosized material and the small size, but when performing an EDS analysis of the surface, its presence was detected (see Figure S2 in the Supplementary Materials). Figure 4b shows the FESEM image of the graphene doped with MnO_2 deposited

on Kapton. Again, a very good coverage of the substrate surface is seen. However, in this case, the surface of the substrate is getting rapidly charged because of the effect of the magnetic field coming from the BSE detector, leading to the formation of very bright areas. Similarly, in the samples on silicon, an EDS analysis (see Figure S3 in the supplementary materials) detected the presence of MnO_2 in the samples deposited over Kapton. Still, the MnO_2 crystals are too small to be seen in the FESEM images, just as for the sensing layer deposited on silicon.

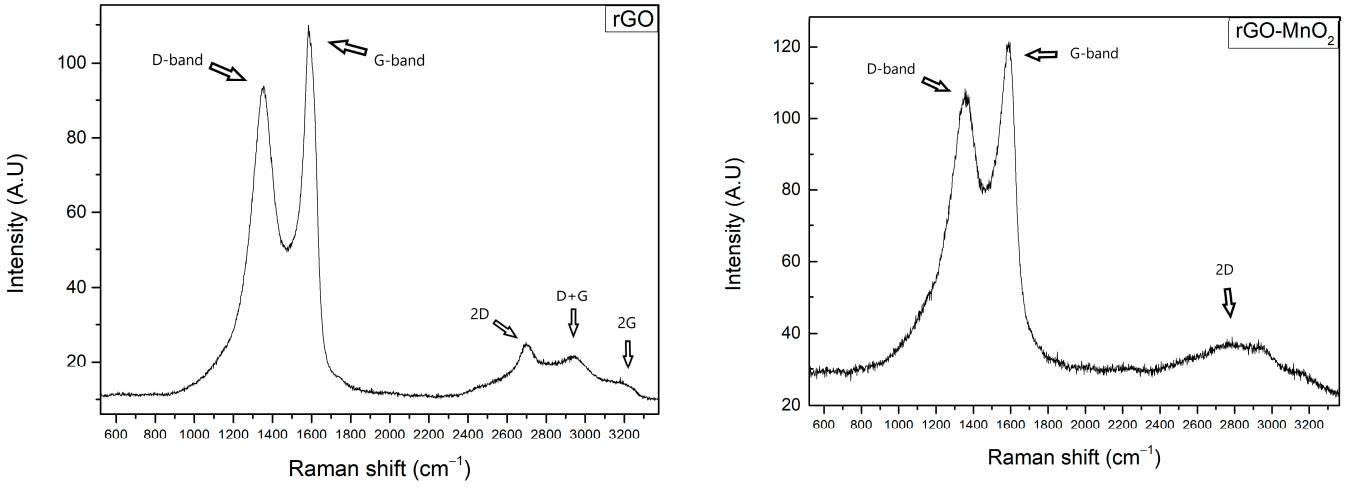

(**a**) (**b**)

Figure 3. (**a**) Raman spectra of rGO and (**b**) Raman spectra of rGO@MnO_2.

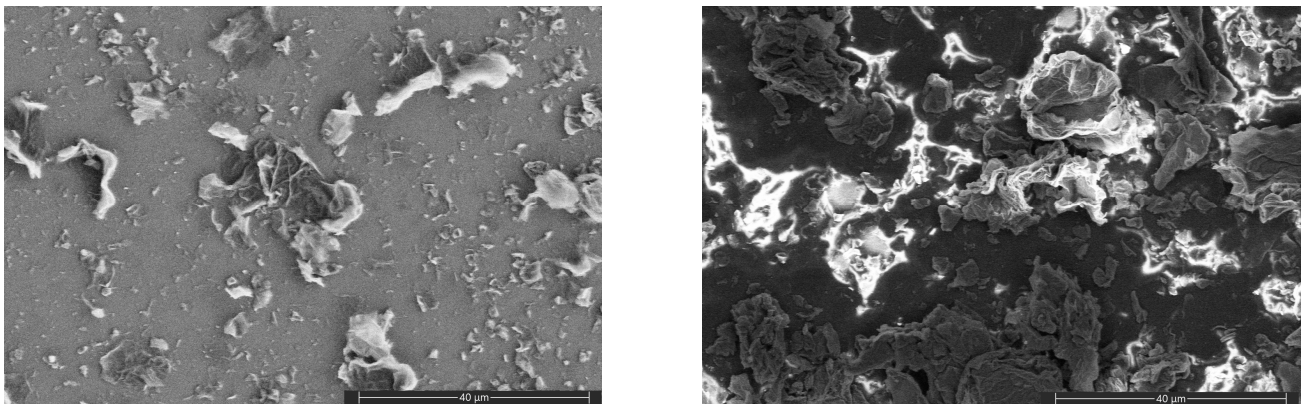

(**a**) (**b**)

Figure 4. FESEM images of (**a**) the surface of the graphene doped with MnO_2 deposited on the silicon substrate and (**b**) the surface of the graphene doped with MnO_2 deposited on the Kapton substrate.

3.1.3. HRTEM

An HR-TEM analysis was conducted to examine better the morphology of the nanosized MnO_2 and its incorporation in the graphene layer. Figure 5a shows an HR-TEM image of layers of graphene in addition to an interesting structure on the top right side; zooming in on this structure (Figure 5b), a sponge-like shaped nanosized material was observed, which was attributed to the MnO_2 after performing an EDS analysis. Moreover, when chemically mapping the chosen area's surface, a high concentration of Mn is located in the same position as the sponge-like structure, proving the presence and the likely shape of the nanosized MnO_2 shown in Figure 5c. Meanwhile, Figure 5d,e shows the EDS mapping of the other present elements, which are O and C, respectively. Moreover, Figure 5f shows an overlay image of all the maps of the elements carbon, manganese and oxygen. The

overlapping of the elements Mn and O maps with the colours blue and red created a pink zone where the nanosized MnO_2 is concentrated. Finally, Figure 5g presents the EDS map spectrum of the same area, showing the elements present in the mapping appearing as Mn with the highest concentration; the other elements, except for C and O, come from the grid of the HRTEM.

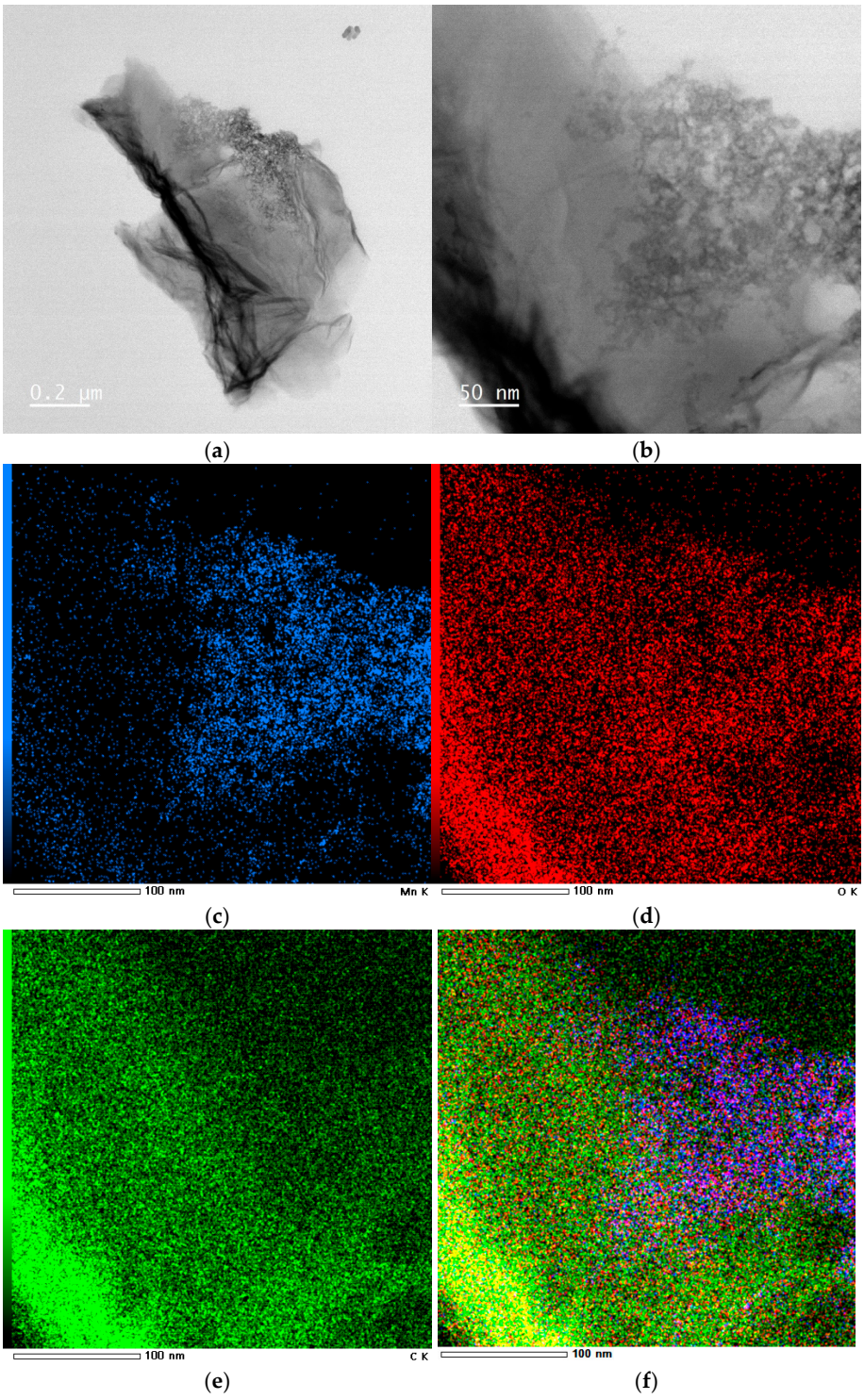

(**a**) (**b**) (**c**) (**d**) (**e**) (**f**)

Figure 5. *Cont.*

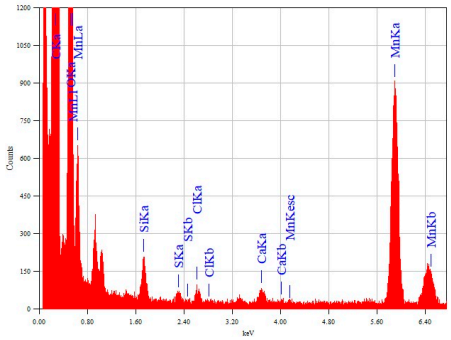

(**g**)

Figure 5. (**a**) HRTEM image of layered graphene doped with nanosized MnO_2; (**b**) a zoomed HRTEM image of a scale of 50 nm of the same material; (**c**) EDS mapping showing Mn concentration on the area of analysis; (**d**) EDS map of O element in the mapped area; (**e**) EDS map of C element in the same mapped area; (**f**) overlay image of all the maps of the elements C (green), O (red) and Mn (blue); (**g**) EDS map spectrum of the studied area.

3.1.4. ATR-IR

Figure 6 shows the ATR-IR spectrum of both rGO@MnO_2 on silicon and Kapton substrates. Examining Figure 6a,b, we can see rGO specific bands for the stretches of C=C and C–O, a specific band for the Mn–OH vibration proving the successful association of Mn and rGO producing MnO_2@rGO and finally, a specific band for the Mn–O vibration. These bands are present in both materials deposited on silicon and on Kapton substrate. The only difference is the presence of the OH band and also the position of the previously mentioned peaks. For the MnO_2@rGO deposited on silicon, the C=C and C–O stretches are located at around 1144 and 1012 cm^{-1}; meanwhile, for the MnO_2@rGO deposited on Kapton, those peaks are located around 1577 and 1017 cm^{-1} [53]. The Mn–OH stretch is located at 784 cm^{-1} for the sensitive material deposited on silicon and at 870 cm^{-1} for the same material on Kapton. The Mn–O stretch is present for the rGO@MnO_2 at 491 cm^{-1}; meanwhile, the material deposited on Kapton is at 501 cm^{-1}. Moreover, Kapton-specific peaks were clearly seen in the spectrum shown in Figure 6b; these peaks were identified and reported in the work of Evie L. et al. [54].

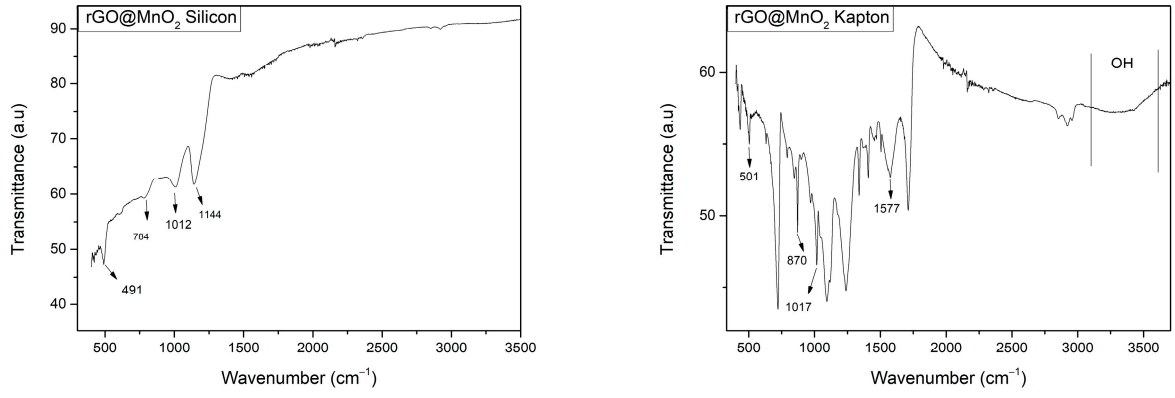

(**a**) (**b**)

Figure 6. ATR-IR spectra of (**a**) rGO@MnO_2 on silicon substrate and (**b**) rGO@MnO_2 on Kapton substrate.

Finally, in the ATR-IR spectrum of the material deposited on Kapton, we can observe a bump between 3000 and 3600 cm^{-1}, specific for the OH stretching vibration, which is absent in the Spectra of the same material deposited on silicon. Thus, the substrate generates differences in the film, and Kapton particularly favours hydroxylation, which has an impact on sensing behaviour.

3.2. Gas Sensing Results

A selection of different toxic gases and vapours was used to study the sensing properties of the pristine rGO and rGO@MnO_2 sensors. First, NO_2 was thoroughly studied with different dilutions ranging from 200 ppb up to 1000 ppb under dry air as well as under ambient moisture conditions (close to real conditions). Sensors were always operated at room temperature. Then, NH_3 was also tested as an interferent gas with a concentration of 50 ppm under the same conditions used for NO_2. The registered baseline resistance of both the materials when conducting these tests for rGO@MnO_2 on silicon is near 100 kΩ while the value is near 6 MΩ when deposited on Kapton. For pristine rGO material films, the baseline resistance over the silicon substrate is near 13.2 kΩ and for the Kapton substrate, it is near 28.5 kΩ. This difference in baseline resistance values of the same material on different substrates is directly affected by the sensitive layer thickness; Figures S4 and S5 show the deposited layers' thickness on top of each substrate. Noticeably, the material on top of silicon has a higher thickness and, thus, a lower resistance value. Meanwhile, materials on Kapton have lower thickness and, thus, higher resistance values. Figure 7a shows the response of the different sensors towards different concentrations of NO_2, and it was noticed that the type of substrate used does not affect the response of the sensitive layer towards the analyte. rGO on silicon and Kapton has almost the same response through the studied range, with an average difference of 0.8%. The same behaviour was also seen for the rGO@MnO_2 sensors, where the average difference between the responses was 0.4%. Moreover, the most important aspect to note is that the sensors based on rGO incorporating MnO_2 show a superior response to the pristine ones (a two-fold increase in response). The loading of rGO with MnO_2 is effective at increasing sensitivity towards NO_2. In fact, rGO@MnO_2 on Kapton exhibits a higher sensitivity of 3% ppm^{-1} compared to the 1% ppm^{-1} for the pristine rGO; meanwhile, for the materials deposited on silicon, the sensitivity of the doped material is slightly better than its pristine counterpart with 1.8% ppm^{-1} for rGO@MnO_2 on silicon and 1.5% ppm^{-1} for on rGO silicon. The sensitivity values were evaluated from the slope of the line obtained from the linear regression of the responses of the sensor towards different concentrations of the gas. Figure 7b shows the resistance changes of the rGO@MnO_2 on silicon substrate for 600 ppb of NO_2, Figure 7c shows the resistance changes of the rGO@MnO_2 on Kapton substrate for 600 ppb of NO_2 at 25% RH, and Figures S6–S8 show the resistance changes of the same material under the same atmosphere but towards different concentrations of the target gas (NO_2).

Further studies were conducted where ambient moisture was introduced via two different methods to check its effect on the sensing properties of the sensors. The first method consisted of using a CEM to obtain 25% RH, and the second method consisted of using a bubbling water glass bottle that was installed between the mass flow and the chamber to humidify the air and the gas to reach a maximum RH of 70%. The ambient temperature was kept constant at 25 °C throughout the measurement period. Figure 8a,b shows the calibration curves for the studied sensors at 25 and 70% of relative humidity, respectively. Comparing the results shown in Figure 8a (dry conditions) and 6a (25% RH), one can notice that the response of the MnO_2-doped rGO sensors under humid conditions increases by a factor of 2.5 than when under dry conditions. For example, the rGO@MnO_2 on Kapton sensor response for NO_2 1000 ppb at 25% humidity is 17.6%, while it is 6.4% under dry conditions. Interestingly, the responses of the pristine rGO sensors at 25% RH were enhanced by factors of 3.5 and 4, reaching similar response intensities to those recorded for MnO_2-doped rGO sensors. For example, rGO on silicon and rGO on Kapton responses to NO_2 1000 ppb were 13.8% and 12.7%, respectively, whereas under a dry atmosphere, their responses were 4.1% and 3.2%, respectively. Sensitivity values were calculated following the slope of the linear regression of the response values towards different dilutions of NO_2 and compiled in Table 3.

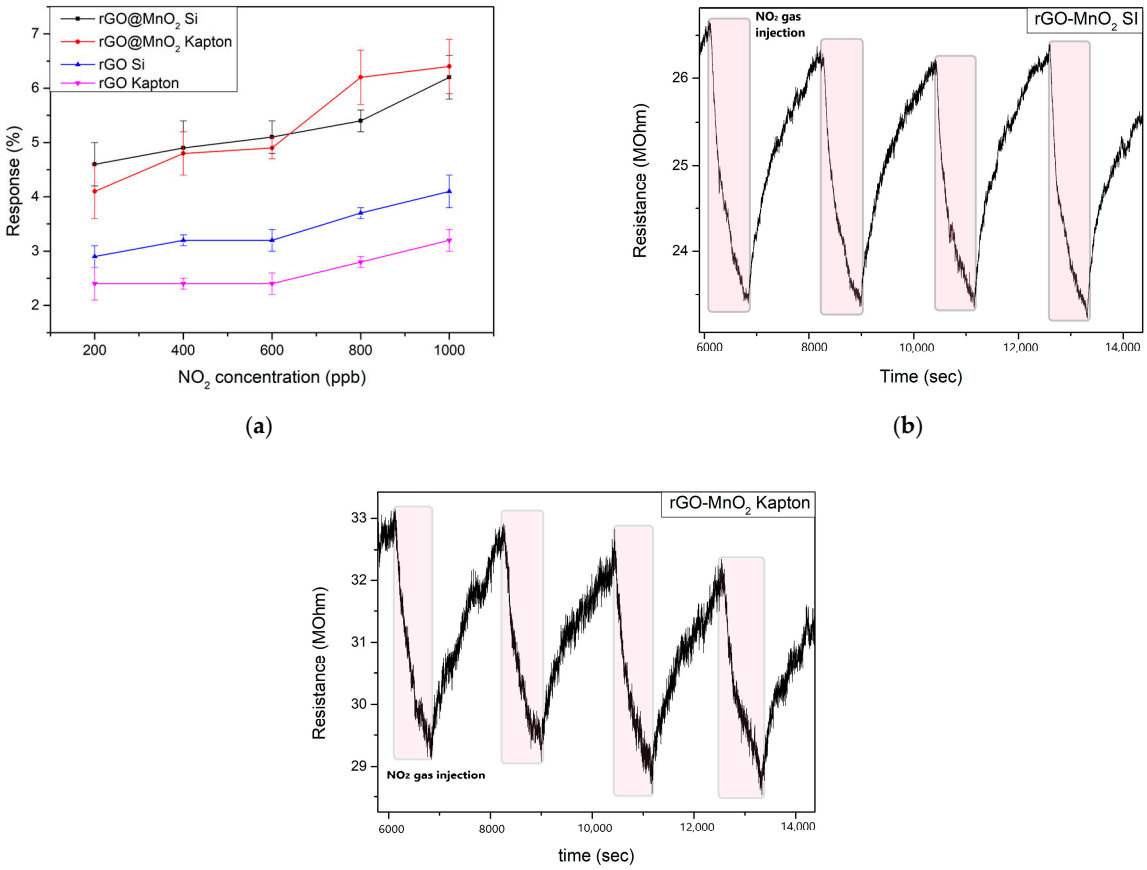

Figure 7. (**a**) Calibration curve of the responses of the fabricated sensors towards different concentrations of NO_2 at room temperature and under dry conditions; (**b**) resistance changes of the rGO@MnO_2 on silicon substrate for 600 ppb of NO_2 at 25% RH; (**c**) resistance changes of the rGO@MnO_2 on Kapton substrate for 600 ppb of NO_2 at 25% RH.

Table 3. Sensitivity values of the different sensors under 25% and 70% relative humidity at room temperature.

Material	Sensitivity (% ppm^{-1})	Relative Humidity (%)
rGO-MnO_2 Silicon	9.8 27.2	25 70
rGO-MnO_2 Kapton	12.4 16.6	25 70
rGO Silicon	10.9 13.5	25 70
rGO Kapton	10.2 14.5	25 70

Meanwhile, Figure 8b reveals the calibration curves of the sensors under 70% ambient moisture. It is noticed that when increasing the concentration of water vapour, the response of the pristine rGO sensors is much more enhanced than the corresponding doped ones, but the increase in the sensitivity is not so significant. When measuring 1000 ppb of NO_2 and increasing the RH levels from 25 to 70%, the response of the pristine rGO sensors is doubled, while the sensitivity just increased by a factor of around 1.3. In the case of the rGO@MnO_2 sensors, the increase in the response is only in the order of a factor of 1.2, but

the increase in the sensitivity is higher than in the previous case, especially for the sensor on the silicon substrate, as can be seen in Table 3.

This behaviour of the pristine rGO layers is expected since the same material was already reported in the literature as a humidity detector, such as in the work of Muhammed et al., where they fabricated rGO and rGO/Fe_2O_3 components for humidity detection and the pristine material showed a high sensitivity towards RH and it increased more with the incorporation of Fe_2O_3 [55]. Zhou et al. also managed to make humidity sensors with the sensitive layer of rGO/SnO_2. Initially, they tested the pristine SnO_2 sensitivity and response towards 75% RH, and they saw these results improve by adding rGO and making rGO/SnO_2 porous film, indicating the fact that rGO is a very sensitive material towards humidity [56]. Although in this work, pristine rGO response towards RH increases with the increase of the humidity level, the doping of rGO with MnO_2 made the response less affected by the RH levels, but the sensitivity increases when the level of humidity increases. Theoretical LOD was calculated following this formula: LOD = 3.3 * (Sy/S), and the values are compiled and shown in Table S3.

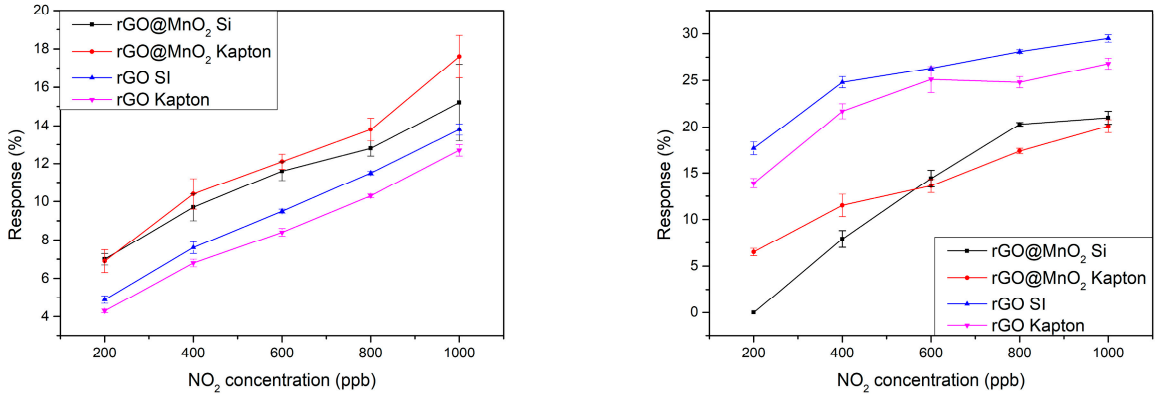

Figure 8. (**a**) calibration curves of the different sensors under 25% relative humidity at room temperature and (**b**) calibration curves under 70% relative humidity at room temperature.

Table 4 compares the results reported here with those of the literature. The sensors we report are more sensitive to NO_2 than those found in the literature. In addition, the concentrations tested in the literature are generally higher than the ones reported here, which indicates that our material is more sensitive in the low ppm concentration range. While most works totally overlook the effect of ambient humidity in the sensing properties, our material is shown to be able to detect NO_2 in a wide range of ambient moisture levels.

Table 4. Comparison of the sensing performance to NO_2 of different materials and rGO-based compounds.

Material	NO_2 Concentration (ppm)	Response (%)	Condition	Sensitivity (%ppm^{-1})	T (°C)	Ref.
Nano-MnO_2/xanthan	7	1.21	Dry	0.17	RT	[57]
δ-MnO_2-Epitaxial Graphene-Silicon Carbide Heterostructures	5	0.27	55% RH	0.14	RT	[58]
Porous MnO_2 /rGO	50	5.9	Dry	0.118	RT	[41]
ZnO/rGO	10	5.1	Dry	0.51	RT	[59]
rGO pomegranate peels	1	3.04	Dry	2.94	100	[60]
Phosphate doped rGO	1	4.5	Dry	4.5	RT	[61]
VO_2/rGO	5	1.63	Dry	0.326	RT	[62]
MnO_2 doped rGO	1	6.2	Dry	9.8	RT	This work
MnO_2 doped rGO	1	21	70% RH	27.2	RT	This work

The selectivity of the different sensors we tested was studied under the same experimental conditions used for NO_2 detection. Different species, namely, CO (50 ppm), NH_3 (50 ppm), H_2 (500 ppm), ethanol (20 ppm) and benzene (1 ppm) under dry conditions for sensors operating at room temperature were measured. Figure 9 shows the responses to these different gases or vapours. As can be seen, none of the sensors showed any response to H_2 and benzene. Noticeably, the inclusion of the nanosized MnO_2 reduced the response towards CO and Ethanol, making it utterly unresponsive to these interfering gases. Therefore, the incorporation of MnO_2 improved the sensor's selectivity. Nevertheless, all the sensors showed very significant responses towards 50 ppm of NH_3.

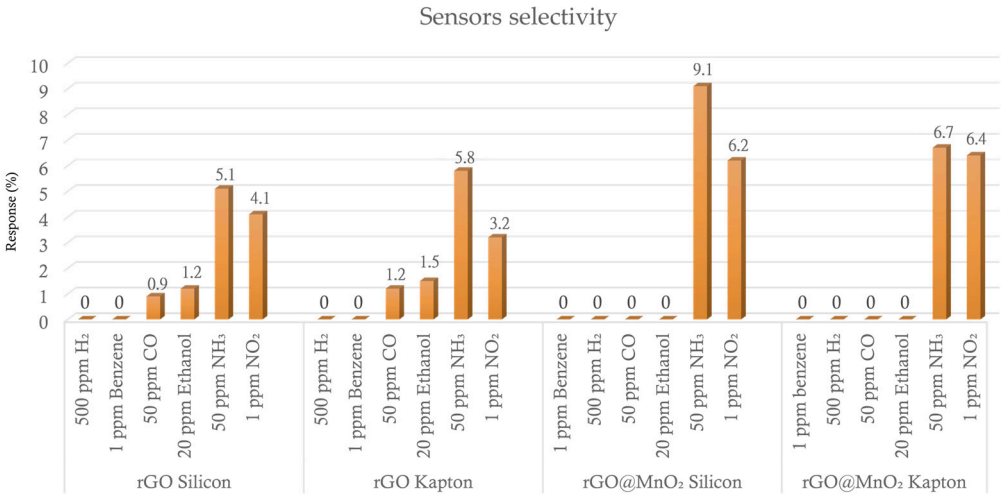

Figure 9. Comparison of the responses of the different sensors towards different gases at dry conditions to study the selectivity of the sensitive layer.

Taking into account the good responses observed for NH_3, the effect of moisture in the sensor responses to this gas was analysed. The sensors were exposed to 50 ppm of NH_3 under different humidity conditions (dry, 25% RH and 50% RH), always at room temperature. Figure 10a shows the responses of the sensors to 50 ppm of ammonia for the three different humidity conditions studied, and Figure 10b shows resistance changes of the sensor pristine rGO on Kapton when exposed to NH_3. As seen in the figure, when exposed to an ammonia analyte, the sensor resistance decreases in contrast to what is expected for a p-type material; this behaviour was explained later in the mechanism part. It was also noticed that the response of the rGO@MnO_2 on the silicon sensor was the highest throughout all the conditions. The response of this sensor reaches a value of 18.5% at 50% RH, which is 4 times higher than the response of the pristine rGO on silicon. rGO@MnO_2 and pristine rGO on Kapton show basically the same behaviour, and the doped one shows a slightly higher response towards NH_3, with values of 6.7% and 5.8% for rGO@MnO_2 and rGO, respectively, under dry conditions, 7.5% and 6% for 25% RH and 8% and 6.7% at 50% RH. Pristine rGO on silicon shows the lowest response values towards ammonia, with a value of 4.6% at 50% RH. In essence, pristine rGO on Kapton and on Silicon substrates shows a linear-like behaviour throughout the different RH levels tested, with very little increase in sensitivity and increasing moisture levels. To have a better understanding of the behaviour of the sensors towards ammonia under humidity, it could be explained as follows: Since we are working in a humid environment, the sensing layers have already adsorbed water molecules on its surface, saturating to an extent the adsorption sites, especially of the pristine rGO layers. Later on, when these layers are exposed to an NH_3 gas flow, another phenomenon happens in the working atmosphere, and it can be attributed to the characteristics of ammonia itself. In fact, both H_2O and NH_3 have a strong tendency to form H bonds. Moreover, the electronegativity of the atoms determines the possibility of forming hydrogen bonds, and since oxygen is more electronegative than nitrogen, the O atom from

H_2O rapidly creates a hydrogen bond with NH_3 [33], as shown in Figure 10c. Therefore, when considering the silicon substrate sensors, the response of the pristine rGO sensor remains practically unchanged because of the phenomenon previously explained, which prevents ammonia molecules from getting adsorbed on the surface. Meanwhile, for the rGO@MnO_2 sensor, the significant increase in the response, despite the occurrence of the hydrogen bonding of the ammonia and water molecules, can be explained by the presence of the nanosized MnO_2, which plays a compensatory role by creating more adsorption sites in the layer, meaning more space for the ammonia and water molecules to be adsorbed also it has been previously reported as a good NH_3 adsorbing agent [63], which explains the increase of the response of the MnO_2@rGO sensor. As for the sensors deposited on Kapton, both pristine rGO and rGO@MnO_2 showing similar behaviour can be explained by the fact that the substrate is made of a very strong hydrophobic material. Therefore, water molecules are getting repelled off of the surface, resulting in poor H_2O adsorption and a low dependency on these sensors for ambient moisture.

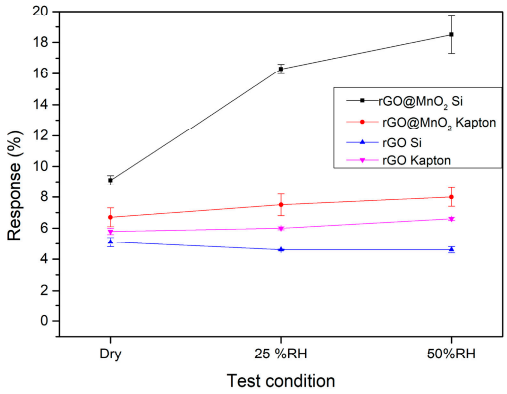

(**a**)

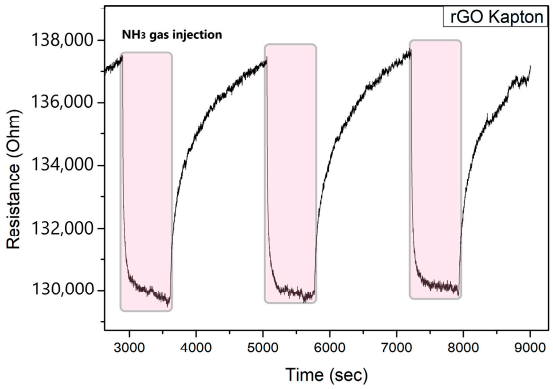

(**b**)

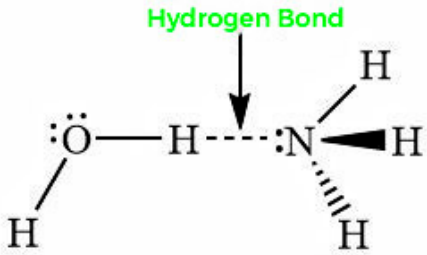

(**c**)

Figure 10. (**a**) Calibration curve of the responses of the fabricated sensors towards different test conditions (Dry, 25% RH and 50% RH); (**b**) resistance changes of the sensor pristine rGO on Kapton when exposed to NH_3 at 25% RH; (**c**) hydrogen bonding of water and ammonia molecules.

To check the position of this work in the literature regarding ammonia detection, a set of data such as response and sensitivity of other materials and sensors analysing NH_3 gas were collected and compiled in Table 5 and put in comparison with our results. Considering the same NH_3 concentration, $NiFe_2O_4$/rGO had a response of 1.17; meanwhile, Pani@MnO_2@rGO had a response of 15.5 while heating up to 100 °C. Both these materials showed lower responses than our work, which was 18.6% at 50% RH. It is true that $FeCo_2O_4$/WO_3/rGO have a slightly higher response of 19.8% at dry conditions, but in this

work, NH_3 concentration is 100 ppm, and the working temperature is 200 °C; meanwhile, we are working at RT and half of the NH_3 concentration.

Table 5. Comparison of the sensing performance to NH_3 of different materials and rGO-based compounds.

Material	NH_3 Concentration (ppm)	Response (%)	Condition	T (°C)	Ref.
PANI@MnO_2@rGO	50	15.5	Dry	100	[44]
$NiFe_2O_4$/rGO	50	1.17	Dry	0	[64]
rGO/WO_3	40	8.03	55% RH	35	[65]
$FeCo_2O_4$/WO_3/rGO	100	19.8	Dry	200	[66]
$CoFe_2O_4$/rGO	25	1.06	Dry	RT	[67]
rGO@MnO_2	50	18.6	50% RH	RT	This work

3.3. Sensing Mechanism

Graphene and its derivatives, such as rGO, are p-type materials, which implies that usually, the interaction between rGO and oxidising gases such as NO_2 causes a change in the local carrier concentration and, therefore, a decrease in graphene-based sensor resistance meanwhile when exposed to reducing gas such as NH_3 an increase in the resistance takes place [68]. Meanwhile, MnO_2 is an n-type nanomaterial, and when exposed to an ambient environment, a chemisorption of the oxygen molecules takes place, capturing electrons from it and releasing different oxygen species such as O_2^-, O^{2-} and O^- [69]. Moreover, the incorporation of the MO_X nanomaterial (in our case, nanosized MnO_2) in the rGO results in the formation of a p-n heterojunction, causing the flow of the electrons from the MnO_2 to rGO, implying the formation of a depletion layer on the area of contact of both materials, also increasing the electron concentration in the rGO and the hole concentration in MnO_2 [70]. The exposure of the rGO@MnO_2 to air leads to the adsorption of oxygen on the surface of the p-n heterojunction material and the transfer of electrons from its conduction band to the oxygen, resulting in the formation of O_2^- ions following these equations [71]:

$$O_2 \text{ gas} \rightarrow O_2 \text{ (ads)}$$

$$O_2 \text{ (ads)} + e^- \rightarrow O_2^- \text{ (ads)}$$

When exposed to NO_2, it gets adsorbed on the rGO@MnO_2 surface and reacts with the oxygen ions and electrons from the layer following this equation, causing the decrease of the resistance of the sensor:

$$NO_2(\text{ads}) + O_2^- \text{ (ads)} + 2e^- \rightarrow NO_2^- + 2O^- \text{ (ads)}.$$

As expected, our material showed the exact same behaviour explained previously, where the baseline resistance of the sensors decreased when put in contact with NO_2 gas and recovered again when the gas flow stopped.

Although NH_3 is a strong reducing gas, the baseline resistance should increase when in contact with the gas, but not in our case, where the resistance of our sensors decreased. This behaviour has been reported previously by A. Umar et al. when exposed to NH_3, the interaction between the analyte and the sensitive layer results in the release of electrons back to the conduction band of the nanosized MnO_2, which is believed to be the cause of the decrease of the resistance of the sensor [41]. This behaviour has been observed also for pristine rGO and was reported in the work of X. Xiao et al. [72]. More interestingly, D. Han et al. comprehensively studied the NH_3 sensing mechanisms, revealing that by changing from a pure air atmosphere to an environment with the presence of NH_3, a significant change in the width of the depletion layer can be induced [73]. Thus, it is worth noting that our sensitive film is essentially p-type owing to the major presence of rGO acting as a transducing element. However, the presence of the MnO_2 doping element, which is

n-type, creates a p-n heterojunction, resulting in a depletion layer. Therefore, when the NH_3 interact with the MnO_2, this probably leads to a decrease in the width of the depletion layer, resulting in a more efficient transport and mobility of charge carriers. Consequently, the conductivity of the film is improved, resulting in the observed decrease of resistance when the sensor is exposed to NH_3 in comparison to a pure air atmosphere.

Finally, graphene-based sensors are well known to be sensitive towards ambient moisture, enhancing its responses [74]. Since the working temperature is at room temperature, water molecules most likely play the role of a mediated adsorption site for the target gas, thus increasing the sensor's sensitivity and responses towards the chosen analyte [75], which is in accordance with the results we obtained, where the responses of the sensors increased under the ambient moisture conditions.

4. Conclusions

Incorporating nanosized MnO_2 in rGO flakes to form a MnO_2@rGO nanomaterial to be integrated into chemoresistive sensors is a novel approach since a very limited number of papers exist in the literature reporting the use of this material as a sensitive layer for gas detection. Additionally, since the same material was deposited on two different substrates (Kapton and silicon), the effect of the substrate material on the morphological and sensing behaviour of the sensing material was thoroughly studied and reported in this work. Our nanomaterial exhibits better performance and properties than other approaches previously reported in the literature, showing a set of very promising results and high responses towards low concentrations of NO_2 and NH_3. When deposited either onto rigid (silicon) or flexible (polyimide) transducing substrates, the material shows good response properties when operated at room temperature and even in the presence of ambient humidity. Furthermore, sensors show very small cross-sensitivity to other species such as hydrogen, ethanol and benzene vapours or carbon monoxide. All these properties make MnO_2@rGO an excellent candidate nanomaterial for the inexpensive, chemoresistive detection of nitrogen dioxide or ammonia in real-life environments using either the flexible substrate for wearable sensors for real-time gas monitoring or using silicon substrate for the possibility of integrating gas sensors in the semiconductor industry.

Supplementary Materials: The following supporting information can be downloaded at: https://www.mdpi.com/article/10.3390/chemosensors12120256/s1, Figure S1: XRD graph of rGO@MnO_2 powder showing the presence and crystalline phase of manganese oxide; Figure S2: The extracted spectrum from the EDS analysis for rGO@MnO_2 on Silicon; Figure S3: The extracted spectrum from the EDS analysis for rGO@MnO_2 on Kapton; Figure S4: Sensitive layer thickness on top of silicon substrate; Figure S5: Sensitive layer thickness on top of Kapton substrate; Figure S6: Resistance changes of the rGO@MnO_2 sensor when exposed to 200 ppb of NO_2; Figure S7: Resistance changes of the rGO@MnO_2 sensor when exposed to 400 ppb of NO_2; Figure S8: Resistance changes of the rGO@MnO_2 sensor when exposed to 800 ppb of NO_2; Table S1: Characteristics of the elements present in the studied sensitive layer; Table S2: Characteristics of the elements present in the studied sensitive layer; Table S3: Calculated theoretical values of LOD for the different sensitive layers at different conditions.

Author Contributions: Conceptualisation, X.V. and J.C.-C.; methodology, M.A.A., X.V.; Software, A.S.-B.; validation, M.A.A.; formal analysis, M.A.A., X.V., J.C.-C.; investigation, M.A.A.; resources, F.S., J.C.S.-C., A.S.-B., S.d.B.-M. and A.G.-G.; data curation, M.A.A.; writing—original draft preparation, M.A.A.; writing—review and editing, J.C.-C., E.L., X.V., S.d.B.-M., A.G.-G. and F.S.; visualisation, M.A.A.; supervision, J.C.-C. and X.V.; project administration, X.V. and E.L.; funding acquisition, X.V. and E.L. All authors have read and agreed to the published version of the manuscript.

Funding: This research was funded in part by MICINN and FEDER grant no. PDC2022-133967-I00 and AGAUR grant no. 2021 SGR 00147. E.L. is supported by the Catalan Institute for Advanced Studies (ICREA) via the 2023 Edition of the ICREA Academia Award. J.C.-C. is supported by the Marie Skłodowska-Curie grant agreement No. 101066282—GREBOS.

Data Availability Statement: Data used in this paper are available upon demand.

Acknowledgments: The authors want to acknowledge Sergi Plana Ruiz for his help and important discussions about the HR-TEM analysis results, Mariana Stefanova Trifonova for her assistance in the FESEM images preparation and Eric Pedrol Ripoll for his help with the Raman analysis.

Conflicts of Interest: The authors declare no conflicts of interest.

References

1. Zhang, C.; Luo, Y.; Xu, J.; Debliquy, M. Room temperature conductive type metal oxide semiconductor gas sensors for NO_2 detection. *Sens. Actuators A Phys.* **2019**, *289*, 118–133. [CrossRef]
2. Chen, Q.; Wang, S.; Bai, S.; Shen, L.; Peng, J.; Zhang, Y.; Cui, X.; Yu, C.; Zhang, R.; Li, Y.; et al. Sub-ppt NH_3 detection by MoS_2@sulfur nanosheets. *J. Alloys Compd.* **2024**, *985*, 174070. [CrossRef]
3. Naseem, N.; Tariq, F.; Malik, Y.; Zahid, W.A.; El-Fattah, A.A.; Ayub, K.; Iqbal, J. Sensing ability of carbon nitride (C_6N_8) for the detection of carbon monoxide (CO) and carbon dioxide (CO_2). *Sens. Actuators A Phys.* **2024**, *366*, 114947. [CrossRef]
4. Namduri, H.; Nasrazadani, S. Quantitative analysis of iron oxides using Fourier transform infrared spectrophotometry. *Corros. Sci.* **2008**, *50*, 2493–2497. [CrossRef]
5. Shi, J.; Jiang, Y.; Duan, Z.; Li, J.; Yuan, Z.; Tai, H. Designing an optical gas chamber with stepped structure for non-dispersive infrared methane gas sensor. *Sens. Actuators A Phys.* **2024**, *367*, 115052. [CrossRef]
6. Okoffo, E.D.; Thomas, K.V. Quantitative analysis of nanoplastics in environmental and potable waters by pyrolysis-gas chromatography–mass spectrometry. *J. Hazard. Mater.* **2024**, *464*, 133013. [CrossRef]
7. Gaiardo, A.; Novel, D.; Scattolo, E.; Crivellari, M.; Picciotto, A.; Ficorella, F.; Iacob, E.; Bucciarelli, A.; Petti, L.; Lugli, P.; et al. Optimization of a Low-Power Chemoresistive Gas Sensor: Predictive Thermal Modelling and Mechanical Failure Analysis. *Sensors* **2021**, *21*, 783. [CrossRef]
8. Sun, K.; Zhan, G.; Zhang, L.; Wang, Z.; Lin, S. Highly sensitive NO_2 gas sensor based on ZnO nanoarray modulated by oxygen vacancy with Ce doping. *Sens. Actuators B Chem.* **2023**, *379*, 133294. [CrossRef]
9. Krishna, K.G.; Umadevi, G.; Parne, S.; Pothukanuri, N. Zinc Oxide based gas sensors and their derivatives: A critical review. *J. Mater. Chem. C* **2023**, *11*, 3906–3925. [CrossRef]
10. Kong, Y.; Li, Y.; Cui, X.; Su, L.; Ma, D.; Lai, T.; Yao, L.; Xiao, X.; Wang, Y. SnO_2 nanostructured materials used as gas sensors for the detection of hazardous and flammable gases: A review. *Nano Mat. Sci.* **2022**, *4*, 339–350. [CrossRef]
11. Liu, P.; Wang, J.; Jin, H.; Ge, M.; Zhang, F.; Wang, C.; Sun, Y.; Dai, N. SnO_2 mesoporous nanoparticle-based gas sensor for highly sensitive and low concentration formaldehyde detection. *RSC Adv.* **2023**, *13*, 2256–2264. [CrossRef] [PubMed]
12. Staerz, A.; Somacescu, S.; Epifani, M.; Kida, T.; Weimar, U.; Barsan, N. WO_3-Based Gas Sensors: Identifying Inherent Qualities and Understanding the Sensing Mechanism. *ACS Sens.* **2020**, *5*, 1624–1633. [CrossRef] [PubMed]
13. Mazur, M.; Kapuścik, P.; Weichbrodt, W.; Domaradzki, J.; Mazur, P.; Kot, M.; Flege, J.I. WO_3 Thin-Film Optical Gas Sensors Based on Gasochromic Effect towards Low Hydrogen Concentrations. *Materials* **2023**, *16*, 3831. [CrossRef] [PubMed]
14. Morrison, S.R. Semiconductor gas sensors. *Sens. Actuators* **1981**, *2*, 329–341. [CrossRef]
15. Schedin, F.; Geim, A.K.; Morozov, S.V.; Hill, E.W.; Blake, P.; Katsnelson, M.I.; Novoselov, K.S. Detection of individual gas molecules adsorbed on graphene. *Nat. Mater.* **2007**, *6*, 652–655. [CrossRef]
16. Novoselov, K.S.; Geim, A.K.; Morozov, S.V.; Jiang, D.; Zhang, Y.; Dubonos, S.V.; Grigorieva, I.V.; Firsov, A.A. Electric field effect in atomically thin carbon films. *Science* **2004**, *306*, 666–669. [CrossRef]
17. Gautam, M.; Jayatissa, A.H. Ammonia gas sensing behaviour of graphene surface decorated with gold nanoparticles. *Solid-State Electron.* **2012**, *78*, 159–165. [CrossRef]
18. Ko, G.; Kim, H.-Y.; Ahn, J.; Park, Y.-M.; Lee, K.-Y.; Kim, J. Graphene-based nitrogen dioxide gas sensors. *Curr. Appl. Phys.* **2010**, *10*, 1002–1004. [CrossRef]
19. Long, H.; Harley-Trochimczyk, A.; Pham, T.; Tang, Z.; Shi, T.; Zettl, A.; Carraro, C.; Worsley, M.; Maboudian, R. High Surface Area MoS_2/Graphene Hybrid Aerogel for Ultrasensitive NO_2 Detection. *Adv. Funct. Mater.* **2016**, *26*, 5158–5165. [CrossRef]
20. Zhang, H.; Feng, J.; Fei, T.; Liu, S.; Zhang, T. SnO_2 nanoparticles-reduced graphene oxide nanocomposites for NO_2 sensing at low operating temperature. *Sens. Actuators B Chem.* **2014**, *190*, 472–478. [CrossRef]
21. Xia, Y.; Wang, J.; Xu, J.-L.; Li, X.; Xie, D.; Xiang, L.; Komarneni, S. Confined Formation of Ultrathin ZnO Nanorods/Reduced Graphene Oxide Mesoporous Nanocomposites for High-Performance Room-Temperature NO_2 Sensors. *ACS Appl. Mater. Interfaces* **2016**, *8*, 35454–35463. [CrossRef] [PubMed]
22. Wu, Z.; Chen, X.; Zhu, S.; Zhou, Z.; Yao, Y.; Quan, W.; Liu, B. Enhanced sensitivity of ammonia sensor using graphene/polyaniline nanocomposite. *Sens. Actuators B Chem.* **2013**, *178*, 485–493. [CrossRef]
23. Karaduman, I.; Er, E.; Çelikkan, H.; Erk, N.; Acar, S. Room-temperature ammonia gas sensor based on reduced graphene oxide nanocomposites decorated by Ag, Au and Pt nanoparticles. *J. Alloys Compd.* **2017**, *722*, 569–578. [CrossRef]
24. Andre, R.; Shimizu, F.; Miyazaki, C.; Riul Jr, A.; Manzani, D.; Ribeiro, S.; Oliveira, O.; Mattoso, L.; Correa, D. Hybrid layer-by-layer (LbL) films of polyaniline, graphene oxide and zinc oxide to detect ammonia. *Sens. Actuators B Chem.* **2016**, *238*, 795–801. [CrossRef]
25. Wang, J.; Rathi, S.; Singh, B.; Lee, I.; Joh, H.; Kim, G. Alternating Current Dielectrophoresis Optimization of Pt-Decorated Graphene Oxide Nanostructures for Proficient Hydrogen Gas Sensor. *ACS App. Mater. Interfaces* **2015**, *7*, 13768–13775. [CrossRef]

26. Esfandiar, A.; Ghasemi, S.; Irajizad, A.; Akhavan, O.; Gholami, M. The decoration of TiO_2/reduced graphene oxide by Pd and Pt nanoparticles for hydrogen gas sensing. *Int. J. Hydrogen Energy* **2012**, *37*, 15423–15432. [CrossRef]
27. Li, D.; Lu, J.; Zhang, X.; Jin, D.; Jin, H. Engineering of ZnO/rGO towards NO_2 Gas Detection: Ratio Modulated Sensing Type and Heterojunction Determined Response. *Nanomaterials* **2023**, *13*, 917. [CrossRef]
28. Fellah, M.F. The reduced graphene oxide/WO_3: Sensing properties for NO_2 gas detection at room temperature. *Diam. Relat. Mater.* **2021**, *119*, 108593. [CrossRef]
29. Thomas, A.; Jeyaprakash, B.G. Selective detection of ammonia by rGO decorated nanostructured ZnO for poultry and farm field applications. *Synth. Met.* **2022**, *290*, 117140. [CrossRef]
30. Naresh, B.; Sreekanth, T.; Krishna, K.G.; Kumar, K.S.; Suma, C.; Yoo, K.; Kim, J. Enhanced ammonia detection using rGO-wrapped $Zn_3V_2O_8$ nanostructures. *Sens. Actuators A Phys.* **2024**, *379*, 115928. [CrossRef]
31. Meng, F.-L.; Guo, Z.; Huang, X.-J. Graphene-based hybrids for chemiresistive gas sensors. *Trends Anal. Chem.* **2015**, *68*, 37–47. [CrossRef]
32. Majhi, S.M.; Mirzaei, A.; Kim, H.W.; Kim, S.S. Reduced Graphene Oxide (rGO)-Loaded Metal-Oxide Nanofiber Gas Sensors: An Overview. *Sensors* **2021**, *21*, 1352. [CrossRef] [PubMed]
33. Tripathi, D.; Chauhan, P.; Rawat, R. A synergistic approach to enhance sensitivity and selectivity of room temperature operable ammonia gas sensor with humidity assistance using RGO/WO_3 nanocomposite. *Nanotechnology* **2023**, *35*, 065503. [CrossRef] [PubMed]
34. Daneshnazar, M.; Jaleh, B.; Eslamipanah, M.; Varma, R.S. Optical and gas sensing properties of TiO_2/RGO for methanol, ethanol and acetone vapors. *Inorg. Chem. Commun.* **2022**, *145*, 110014. [CrossRef]
35. Abideen, Z.U.; Kim, H.W.; Kim, S.S. An ultra-sensitive hydrogen gas sensor using reduced graphene oxide-loaded ZnO nanofibers. *Chem. Commun.* **2015**, *51*, 15418–15421. [CrossRef] [PubMed]
36. Lee, J.-H.; Katoch, A.; Choi, S.-W.; Kim, J.-H.; Kim, H.W.; Kim, S.S. Extraordinary Improvement of Gas-Sensing Performances in SnO_2 Nanofibers Due to Creation of Local p–n Heterojunctions by Loading Reduced Graphene Oxide Nanosheets. *ACS App. Mater. Interfaces* **2015**, *7*, 3101–3109. [CrossRef]
37. Hingangavkar, G.M.; Kadam, S.A.; Ma, Y.-R.; Bandgar, S.S.; Mulik, R.N.; Patil, V.B. Tailored formation of WO_3-rGO nanohybrids for dependable low temperature NO_2 sensing. *Ceram. Int.* **2023**, *49*, 38866–38876. [CrossRef]
38. Zhang, Q.Z.; Zhang, D.; Miao, Z.C.; Zhang, X.L.; Chou, S.L. Research Progress in MnO-Carbon Based Supercapacitor Electrode Materials. *Small* **2018**, *14*, e1702883. [CrossRef]
39. Wu, M.; Hou, P.; Dong, L.; Cai, L.; Chen, Z.; Zhao, M.; Li, J. Manganese dioxide nanosheets: From preparation to biomedical applications. *Int. J. Nanomed.* **2019**, *14*, 4781–4800. [CrossRef]
40. Malook, K.; Khan, H.; Shah, M.; Haque, I.-U. Highly selective and sensitive response of Polypyrrole–MnO_2 based composites towards ammonia gas. *Polym. Compos.* **2019**, *40*, 1676–1683. [CrossRef]
41. Zhang, H.; Ou, K.; Guan, R.; Cao, Y.; Sun, Y.; Li, X. A Highly Sensitive Room-Temperature NO_2 Gas Sensor based on Porous MnO_2 /rGO Hybrid Composites. *Curr. Nanosci.* **2022**, *19*, 401–409. [CrossRef]
42. Zöpfl, A.; Lemberger, M.-M.; König, M.; Ruhl, G.; Matysik, F.-M.; Hirsch, T. Reduced graphene oxide and graphene composite materials for improved gas sensing at low temperature. *Faraday Discuss* **2014**, *173*, 403–414. [CrossRef] [PubMed]
43. Ghosal, S.; Bhattacharyya, P. Fabrication, Characterization, and Gas Sensing Performance of Pd, RGO, and MnO_2 Nanoflowers-Based Ternary Junction Device. *IEEE Trans. Electron Devices* **2019**, *66*, 3982–3987. [CrossRef]
44. Umar, A.; Akbar, S.; Kumar, R.; Ahmed, F.; Ansari, S.A.; Ibrahim, A.A.; Alhamami, M.A.; Almehbad, N.; Algadi, H.; Almas, T.; et al. Unveiling the potential of PANI@MnO_2@rGO ternary nanocomposite in energy storage and gas sensing. *Chemosphere* **2024**, *349*, 140657. [CrossRef] [PubMed]
45. Rezaei, I.; Haghverdi, A.B.; Soldoozy, A.; Aghaee, T.; Biabanifard, S. Wearable Kapton graphene biosensor for detection of toxic gases. *J. Hazard. Mater. Adv.* **2024**, *15*, 100452. [CrossRef]
46. Yin, F.; Wu, S.; Wang, Y.; Wu, L.; Yuan, P.; Wang, X. Self-assembly of mildly reduced graphene oxide monolayer for enhanced Raman scattering. *J. Solid State Chem.* **2016**, *237*, 57–63. [CrossRef]
47. Hurtado, R.B.; Cortez-Valadez, M.; Aragon-Guajardo, J.R.; Cruz-Rivera, J.J.; Martínez-Suárez, F.; Flores-Acosta, M. One-step synthesis of reduced graphene oxide/gold nanoparticles under ambient conditions. *Arab. J. Chem.* **2020**, *13*, 1633–1640. [CrossRef]
48. Yavuz, S.; Bandaru, P.R. Ag nanowire coated reduced graphene oxide/n-silicon Schottky junction based solar cell. In Proceedings of the IEEE Conference on Technologies for Sustainability (SusTech), Phoenix, AZ, USA, 9–11 October 2016; pp. 265–269. [CrossRef]
49. Hidayah, N.M.S.; Nur, H.; Liu, W.W.; Lai, C.W.; Noriman, N.Z.; Khe, C.-S.; Hashim, U.; Lee, H.C. Comparison on graphite, graphene oxide and reduced graphene oxide: Synthesis and characterization. *AIP Conf. Proc.* **2017**, *1892*, 150002.
50. Ma, B.; Rodriguez, R.D.; Ruban, A.; Pavlov, S.; Sheremet, E. The correlation between electrical conductivity and second-order Raman modes of laser-reduced graphene oxide. *Phys. Chem. Chem. Phys.* **2019**, *21*, 10125–10134. [CrossRef]
51. Sharma, M.; Rani, S.; Pathak, D.K.; Bhatia, R.; Kumar, R.; Sameera, I. Temperature dependent Raman modes of reduced graphene oxide: Effect of anharmonicity, crystallite size and defects. *Carbon* **2021**, *184*, 437–444. [CrossRef]
52. Rajguru, G.M.; Mishra, R.K.; Kharat, P.B.; Khirade, P.P. Structural, microstructural and optical characteristics of rGO-ZnO nanocomposites via hydrothermal approach. *Opt. Mater.* **2024**, *154*, 115720. [CrossRef]

53. Papadopoulou, E.; Morselli, D.; Prato, M.; Barcellona, A.; Athanassiou, A.; Bayer, I.S. An Efficient Pure Polyimide Ammonia, Sensor. *J. Mater. Chem. C* **2016**, *4*, 7790–7797. [CrossRef]
54. Susee, S.K.; Sandhya, S.; Kumar, M.S.; Chidhambararajan, B. Reduced graphene oxide–MnO_2 nanocomposites by hydrothermal method for histamine sensor and photocatalytic activity. *J. Mater. Sci. Mater. Electron.* **2024**, *35*, 1–12. [CrossRef]
55. Muhammad, Y.; Shah, M.; Safi, M.A.; Khattak, S.G.; Aziz, A.; Hassan, H. highly selective and sensitive humidity sensor using reduced graphene oxide-based iron oxide nanocomposites. *Mater. Sci. Eng.* **2024**, *303*, 117324. [CrossRef]
56. Li, Z.; Gardner, D.W.W.; Xia, Y.; Zhao, S.; Pan, A.; Goel, N.; Bart, S.; Liu, C.; Yi, J.; Carraro, C.; et al. Ordered porous RGO/SnO_2 thin films for ultrasensitive humidity detection. *J. Mater. Chem. C Mater.* **2023**, *11*, 9586–9592. [CrossRef]
57. Fahmy, A.; Saeed, A.M.; Dawood, U.; Abdelbary, H.; Altmann, K.; Schönhals, A. Nano-MnO_2/xanthan gum composite films for NO_2 gas sensing. *Mater. Chem. Phys.* **2023**, *296*, 127277. [CrossRef]
58. Pedowitz, M.D.; Kim, S.; Lewis, D.I.; Uppalapati, B.; Khan, D.; Bayram, F.; Daniels, K.M. Fast Selective Sensing of Nitrogen-Based Gases Utilizing δ -MnO_2-Epitaxial Graphene-Silicon Carbide Heterostructures for Room Temperature Gas Sensing. *J. Microelectromech. Syst.* **2020**, *29*, 846–852. [CrossRef]
59. Lu, J.; Li, D.; Chen, X. ZnO/reduced graphene oxide nanocomposite with synergic enhanced gas sensing performance for the effective detection of NO_2 at room temperature. *J. Nanopart.* **2022**, *24*, 265. [CrossRef]
60. Kacem, K.; Ameur, S.; Casanova-Chafer, J. Bio-reduction of graphene oxide using pomegranate peels for NO_2 sensing and photocatalysis applications. *J. Mater. Sci. Mater. Electron.* **2022**, *33*, 16099–16112. [CrossRef]
61. Hasanov, B.E.; Casanova-Chafer, J.; Deokar, G.; Gouveia, J.D.; Nematulloev, S.; Gomes, J.R.; Llobet, E.; Costa, P.M. Amplified sensing of nitrogen dioxide with a phosphate-doped reduced graphene oxide powder. *Carbon* **2024**, *226*, 119207. [CrossRef]
62. Liang, J.; Wu, W.; Lou, Q. Room temperature NO_2 sensing performance enhancement of VO_2(B) composited rGO structure. *J. Mater. Sci. Mater. Electron.* **2022**, *33*, 15473–15482. [CrossRef]
63. Sovizi, M.R.; Mirzakhani, S. highly sensitive detection of ammonia gas by 3D flower-like ϒ-MnO_2 nanostructure chemiresistor. *J. Taiwan Inst. Chem. Eng.* **2020**, *111*, 293–301. [CrossRef]
64. Ganesan, M.; Ganapathi, B.; Parasuraman, B.; Thangavelu, P. Sensitivity enhancement of ammonia gas sensor based on $NiFe_2O_4$/rGO nanocomposite. *Chem. Phys. Impact* **2024**, *8*, 100616. [CrossRef]
65. Jeevitha, G.; Abhinayaa, R.; Mangalaraj, D.; Ponpandian, N.; Meena, P.; Mounasamy, V.; Madanagurusamy, S. Porous reduced graphene oxide (rGO)/WO_3 nanocomposites for the enhanced detection of NH_3 at room temperature. *Nanoscale Adv.* **2019**, *1*, 1799–1811. [CrossRef]
66. Zhang, H.; Li, Y.; Yuan, Z.; Lei, Y.; Li, X.; Meng, F. Enhanced Ammonia Sensing Performance Based on $FeCo_2O_4$/WO_3/rGO Ternary Nanocomposites. *IEEE Sens. J.* **2023**, *23*, 25698–25707. [CrossRef]
67. Ganesan, M.; Ganapathi, B.; Govindasamy, P.; Parasuraman, B.; Shanmugam, P.; Boddula, R.; Pothu, R.; Thangavelu, P. $CoFe_2O_4$/rGO nanocomposite: Synthesis and enhanced ammonia gas sensing properties at room temperature. *Results Chem. Chem.* **2024**, *7*, 101342. [CrossRef]
68. Alouani, M.A.; Casanova-Cháfer, J.; Güell, F.; Peña-Martín, E.; Ruiz-Martínez-Alcocer, S.; de Bernardi-Martín, S.; García-Gómez, A.; Vilanova, X.; Llobet, E. ZnO-Loaded Graphene for NO_2 Gas Sensing. *Sensors* **2023**, *23*, 6055. [CrossRef]
69. Umar, A.; Ibrahim, A.A.; Kumar, R.; Albargi, H.; Zeng, W.; Alhmami, M.A.M.; Alsaiari, M.A.; Baskoutas, S. Gas sensor device for high-performance ethanol sensing using α-MnO_2 nanoparticles. *Mater. Lett.* **2021**, *286*, 129232. [CrossRef]
70. Chatterjee, S.G.; Chatterjee, S.; Ray, A.K.; Chakraborty, A.K. Graphene–metal oxide nanohybrids for toxic gas sensor: A review. *Sens. Actuators B Chem.* **2015**, *221*, 1170–1181. [CrossRef]
71. Zhang, D.; Liu, A.; Chang, H.; Xia, B. Room-temperature high-performance acetone gas sensor based on hydrothermal synthesized SnO_2-reduced graphene oxide hybrid composite. *RSC Adv.* **2015**, *5*, 3016–3022. [CrossRef]
72. Xiao, X.; Jin, W.; Tang, C.; Qi, X.; Li, R.; Zhang, Y.; Zhang, W.; Yu, X.; Zhu, X.; Ma, Y.; et al. Thermal reduced graphene oxide-based gas sensor for rapid detection of ammonia at room temperature. *J. Mater. Sci.* **2023**, *58*, 11016–11028. [CrossRef]
73. Han, D.; Wang, Y.; Wang, Y.; Duan, Q.; Li, D.; Ge, Y.; He, X.; Zhao, L.; Wang, W.; Sang, S. Machine-learning-assisted n-GaN-Au/PANI gas sensor array for intelligent and ultra-accurate ammonia recognition. *Chem. Eng. J.* **2024**, *495*, 153705. [CrossRef]
74. Lv, C.; Hu, C.; Luo, J.; Liu, S.; Qiao, Y.; Zhang, Z.; Song, J.; Shi, Y.; Cai, J.; Watanabe, A. Recent Advances in Graphene-Based Humidity Sensors. *Nanomaterials* **2019**, *9*, 422. [CrossRef]
75. Casanova-Cháfer, J.; Navarrete, E.; Noirfalise, X.; Umek, P.; Bittencourt, C.; Llobet, E. Gas Sensing with Iridium Oxide Nanoparticle Decorated Carbon Nanotubes. *Sensors* **2019**, *19*, 113. [CrossRef]